Solar Physics (2021) 296:89
https://doi.org/10.1007/s11207-021-01827-z

HAWC as a Ground-Based Space-Weather Observatory

C. Alvarez · J.R. Angeles Camacho · J.C. Arteaga-Velázquez · K.P. Arunbabu · D. Avila Rojas · V. Baghmanyan et al. ***[full author details at the end of the article]***

Received: 27 October 2020 / Accepted: 22 April 2021 / Published online: 10 June 2021

Abstract
The High Altitude Water Cherenkov (HAWC) gamma-ray observatory is located close to the equator (latitude 18° N), at an altitude of 4100 m above sea level. HAWC has 295 water Cherenkov detectors (WCD), each containing four photomultiplier tubes (PMT). The main purpose of HAWC is the determination of the energy and arrival direction of very high energy gamma rays produced by energetic processes in the universe, HAWC also has a scaler system which counts the arrival of secondary particles to the detector. In this work we show that the scaler system of HAWC is an ideal instrument for solar modulation and space-weather studies due to its large area and high sensitivity. In order to prepare the scaler system for low energy heliospheric studies, we model and correct the efficiency variation of each PMT of the array, which result in a capability to measure variations $> 0.01\%$ with high accuracy. Using the singular value decomposition method, we correct the rate deviations of all PMTs of the array, due to changes in efficiency, gain and operational voltage. We isolate and remove the atmospheric modulations of the PMTs count rates measured by the TDC-scaler data acquisition system. In particular, the atmospheric pressure at the HAWC site exhibits an oscillating behavior with a period of $\sim$12 hours and we make use of this periodic property to estimate the pressure coefficients for the HAWC TDC-scaler system. These corrections performed on the TDC-scaler system make the HAWC TDC-scaler system an ideal instrument for solar modulation and space-weather studies. As examples of this capability, we present the preliminary analysis of the solar modulation of cosmic rays at three time scales observed by HAWC, with an unprecedented accuracy.

Keywords Cosmic rays · Atmospheric pressure modulation · Solar modulation · Fast Fourier transform

1. Introduction

The intensity modulation of galactic cosmic rays (GCRs) observed by ground-based instruments has been a topic of interest for decades (Forbush, 1954; Burlaga et al., 1985; Venkatesan and Badruddin, 1990; Kudela et al., 2000; Subramanian et al., 2009; Arunbabu et al., 2013, 2015). These modulations can be classified as solar modulations whose origin depends upon the solar activity, or as atmospheric modulations where the variation of properties like pressure and temperature of the atmosphere causes changes in the observed GCR intensity. Regarding its solar origin, the space-weather transient phenomena like solar flares, coronal mass ejections (CMEs), co-rotating interaction regions (CIRs), and high-speed solar

wind streams cause significant changes in the GCR intensity, making this modulation a useful tool to study the properties of the space-weather transient events (Richardson, Cane, and Cliver, 2002; Kudela et al., 2000; Subramanian et al., 2009; Arunbabu et al., 2013, 2015). In particular, an Earth-directed CME along with its associated shock traveling through the interplanetary medium can produce significant variation in the cosmic ray intensity such as precursor events, Forbush decreases (FDs), and ground-level enhancements (GLEs) (Kudela et al., 2000; Subramanian et al., 2009; Arunbabu et al., 2013). Furthermore, the large scale helical structure of the magnetic field of the so called "magnetic clouds" is able to guide the GCR flux causing anisotropies (Akiyama et al., 2020) that can be used to explore these magnetic structures. The periodic nature of solar phenomena, such as the 27 d solar rotation, 11 yr activity cycle, and 22 yr solar magnetic cycle, will also modulate the GCR intensity (Forbush, 1954; Venkatesan and Badruddin, 1990). Also, the rotation of the Earth in the ambient solar wind results in a periodic variation in the GCR intensity due to axial asymmetry in the geomagnetic environment. This is observed by ground-based instruments and is known as the solar diurnal variation, with a periodicity of 1 solar day (Mohanty et al., 2013). The solar modulations observed are mainly due to the change of primary GCR flux with energies <100 GeV, whereas the atmospheric modulations are due to the change in interaction and decay of secondary particles by virtue of the change in atmospheric properties such as pressure, temperature and density (Mohanty et al., 2016; Arunbabu et al., 2017). As both modulations are present in the observed flux, in order to have effective and accurate solar modulation studies it is more than essential to identify these atmospheric modulations and make an accurate correction.

When a GCR reach the top of the atmosphere and interacts with the ambient atmospheric nuclei, it produces a secondary particle flux, which propagate downwards (Greisen, 1960) forming an air shower which is detected by the ground-based detectors. In the early stages, the neutrons and mesons (pions and kaons) are the major contributors of the produced secondaries. Neutrons have a relatively longer lifetime (~ 15 min) hence the majority of them survive down to ground level. The charged mesons decay because of their short lifetime and produce muons, whereas the neutral pions decay to electrons, positrons and γ rays. Because of their weak interactions, most of these muons survive down to ground level. Therefore, a dominant fraction of secondary cosmic rays detected at ground-level are constituted by the muons, which are largely produced higher up in the atmosphere at altitudes ≥ 6 km (Arunbabu et al., 2017). The mean energy of the muon spectrum at sea-level is ~ 4 GeV, which is almost flat for energies below 1 GeV then steepens gradually to reflect the primary spectrum up to 10 GeV range and steepen further at higher energies (Nakamura et al., 2010). The flux of muon at sea-level is $\sim 70\ \mathrm{m^{-2}\,s^{-1}\,sr^{-1}}$ (Olive, 2014) which increases slowly with higher altitudes. The muon flux observed has a zenith angle (Θ) dependence which varies proportionally to $\cos^2(\Theta)$ at GeV energies (Grieder, 2001; Achard et al., 2004). Therefore, a large area detector located at high altitude and capable to observe both components (electromagnetic and muonic) of the air showers constitutes a great instrument to study GCR modulations.

The work described in this paper explains the various corrections applied on HAWC TDC-scaler system to make it ready for solar modulation and space weather studies. A detailed description of HAWC experiment is given in the upcoming Section 2, followed by a description of how effectively we perform the efficiency variation of each PMT/WCD in the experiment to achieve the high accuracy of measurement in Section 3. The methods used to estimate the pressure coefficient are explained in Section 4 (a preliminary version of these methods was presented in the International Cosmic Ray Conference (ICRC 2019, Arunbabu, Lara, and Ryan, 2019) and Section 5 explains the successful application of this

coefficients for pressure correction. Finally in the discussion we show how these corrections make the data suitable for solar modulation studies and present initial examples of the relation between the solar wind parameters and the observed modulations such as solar diurnal anisotropy, and short/long-term solar modulations.

2. HAWC Observatory

The High Altitude Water Cherenkov (HAWC) observatory is located at an altitude of 4100 m above sea level and on a comparatively plain land near the saddle region between the Sierra Negra and Pico de Orizaba, in Puebla, Mexico, with latitude 18°59′41″ N, longitude 97°18′30.6″ W. This observatory consists of 300 water Cherenkov detectors (WCD) out of which 295 were operational in 2016. Each WCD is 7.3 m in diameter and 4.5 m in depth. The 295 WCDs are spread over an area of 22 000 m^2. Each of these WCDs is filled with filtered water and instrumented with four photomultiplier tubes (PMTs). These PMTs are designed in a specific manner with the 10-inch Hamamatsu R7081-02[1] PMT positioned at the center of the WCD and three 8-inch Hamamatsu R5912[1] PMTs are arranged around this central one making an equilateral triangle of side 3.2 m.

HAWC employs two different data acquisition (DAQ) systems. The main DAQ system measures arrival times and time over threshold of PMT pulses (Abeysekara et al., 2018). This information is used for the reconstruction of air showers to estimate the arrival direction and energy of the primary particles. The electronics are based on time to digital converters (TDC). The main DAQ also has a TDC-scaler system which counts independently the hits of each PMT ($R1$) and the coincidences of 2, 3 and 4 PMTs (in an individual WCD), called multiplicity $M2$, $M3$ and $M4$, respectively, during a time window of 30 ns and with a cadence of 25 ms. The secondary DAQ, called the hardware scaler system, consists of a counting system that registers each time the PMT hit registers more than 1/4 photoelectron charge. This simpler system together with the TDC-scalers allows one to measure primary particles below the energies of reconstructable showers. The scaler systems are intended for monitoring transient gamma-ray phenomena such as gamma-ray bursts (GRBs). These systems are also well suited for studying the solar modulations in cosmic rays. In this analysis, we will be using data from the TDC-scaler system.

3. Efficiency Correction in HAWC TDC-Scaler System

The HAWC TDC-scaler system collects data from all the 1180 PMTs in the 295 WCDs, although HAWC uses two different size PMTs, 10-inch one at the center and 8-inch ones at the corners of an equilateral triangle. Therefore, the mean rates of PMTs ($< R1 >$) are different. There are variations in mean rates of 10 and 8 inch PMTs, which is due to their effective area and change in their quantum efficiency. Apart form this, the rate of each PMT depends upon its gain, operation voltage, and the quantum efficiency (Abeysekara, 2012). These mean rates have a span over a range of $\sim 15-60$ kHz as shown in Figure 1.

Besides the spread in mean rate, each PMT have its own variation in efficiency due to the change in its quantum efficiency caused by the aging process. Also there are changes associated to adjustments of the operating voltage. In order to achieve the statistical accuracy promised by the experiment it is necessary to make corrections for these efficiency

[1] https://www.hamamatsu.com/resources/pdf/etd/LARGE_AREA_PMT_TPMH1376E.pdf.

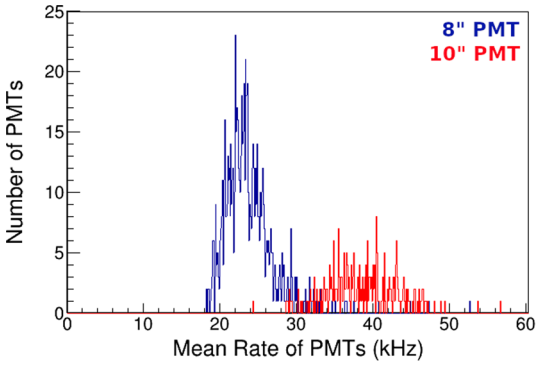

Figure 1 Distribution of the mean rate ($< R1 >$) of 1180 PMTs in HAWC. Distribution of 10 inch PMTs are shown in red color and that of 8 inch are shown in blue color.

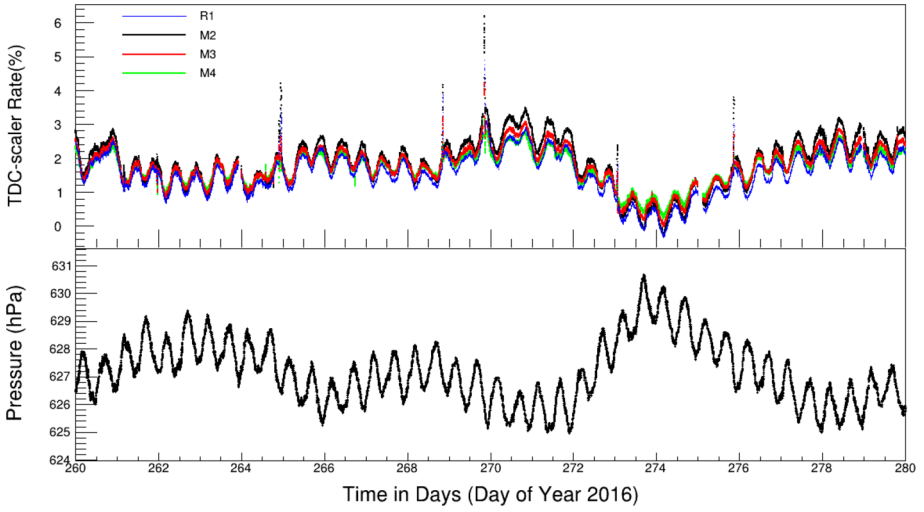

Figure 2 The top panel shows the efficiency corrected combined HAWC TDC-scaler data (1 minute averaged) R_1 and the multiplicity rates R_{M2}, R_{M3}, and R_{M4}. The bottom panel shows the ambient pressure at the HAWC site.

variations. This efficiency correction was achieved by strict monitoring of variation of each PMTs and WCDs for the case of multiplicities. We choose the best 30 PMTs and WCDs by considering their relative spread to each other after self normalizing their daily rate by the rate of the first day in the year. A recurrent iterative analysis was used to eliminate PMTs causing higher standard deviations. The rates of chosen best PMTs and WCDs were used to estimate the 'reference rate' using 'singular value decomposition' method (Mohanty et al., 2017). The obtained 'reference rate' was used to correct the efficiency of each PMT and WCD by modeling the relative variation using a fourth order polynomial. These model-fits were further used to correct the efficiency variation of each PMT and WCD. The efficiency corrected rates of PMTs (for $R1$) and tanks (for multiplicities) were combined/averaged, in this way we acquired the required accuracy of measurement ($< 0.01\%$ for one minute resolution data) of HAWC TDC-scaler system.

We use the HAWC TDC-scaler system 1-minute averaged rate from all 1180 PMTs which will be called R_1. Also, we use the 1-minute averaged rates for multiplicities $M2$, $M3$ and

$M4$, which will be represented as R_{M2}, R_{M3} and R_{M4}, respectively. It should be noted that the R_1 rates are dominated by secondary electromagnetic particles along with the muons. By virtue of its high altitude and latitudinal location comparatively closer to the equator, HAWC is having a geomagnetic vertical cut-off rigidity of 7.9 GV (Lara, 2013). This cut-off rigidity was estimated using a back-tracing method (Smart and Shea, 2005), where we used the concept that the trajectory of protons arriving at Earth is the same as that of anti-protons ($\bar{p}$) of the same rigidity leaving Earth. The trajectory of a proton of a given rigidity was simulated by launching a $\bar{p}$ of same rigidity moving away from the Earth. Their trajectories are traced (Smart and Shea, 2005) in the geomagnetic field modeled by IGRF12 (Thébault et al., 2015), which represents a secular geomagnetic field, we note that a detailed analysis of the cut-off rigidity during geomagnetic disturbed times (Asorey, Núñez, and Suárez-Durán, 2018) is out of the scope of this paper. The minimum rigidity of the $\bar{p}$ escaping from the Earth varies inside a small range, therefore the mean rigidity of this range defines the cut-off rigidity at that location. On the other hand the median rigidity of observation for different multiplicities were estimated using HAWC's standard Monte Carlo simulations. These simulations relies on Corsika (Heck et al., 1998) to simulate the extensive air showers in great detail and obtain a very comprehensive set of secondaries reaching ground level. Followed by this a GEANT4 (Agostinelli et al., 2003) based model is used to estimate the detector response by propagating the secondary particles through the HAWC detector to the PMTs (Enriquez-Rivera, Lara, and Caballero-Lopez, 2015). A similar simulation chain but for two LAGO detectors is presented in Asorey, Núñez, and Suárez-Durán (2018). The estimated values of median rigidity for R_1, M_2, M_3 and M_4 are, respectively, 41.97, 41.46, 42.28, and 45.04 GV. The efficiency corrected rates of HAWC TDC-scaler system for the year 2016 have average rates of $< R_1 >= 23.39$ kHz, $< R_{M2} >= 8.06$ kHz, $< R_{M3} >= 5.69$ kHz, and $< R_{M4} >= 4.35$ kHz. Since the spread of the mean rates is large, we consider the percentage variation ($\frac{R_1 - < R_1 >}{< R_1 >} \times 100$) of rates for each PMT in our analysis. By considering the percentage deviation, all PMTs ($10''$ and $8''$) will have similar variation irrespective of their mean rate. Similarly, the percentage deviations were also used for the multiplicity rates. We note that the effects of physical phenomena like solar modulation and atmospheric modulation will be seen uniformly by all the PMTs/WCDs, hence the percentage variations due to these effects will be the same for all PMTs/WCDs irrespective of their gain. Different PMTs have different noise due to the thermal effects and natural radioactivity, but this noise level is much less than the signal due to secondary particles. The efficiency corrected combined HAWC TDC-scaler system is having a statistical accuracy $< 0.01\%$ per minute, and can measure any variations larger than this limit with accuracy. The efficiency corrected combined TDC-scaler rates are shown in Figure 2 for a short period of time of 20 days arbitrarily chosen from the day of the year 260 to 280 for the year 2016. The data clearly shows the atmospheric pressure modulations in it, also we can see sudden short time increases in the rate, which are associated with the atmospheric electric field events (Jara Jimenez et al., 2019). The anti-correlation between the TDC-scaler rate and the pressure is always present, as instance, this anti-correlation but during a different period of observation can be seen in Arunbabu, Lara, and Ryan (2019).

4. Determining Pressure Dependence

The change in mass of the air column above the detector is reflected as the variation of the atmospheric pressure, which in turn results in a synchronous variation in the observed

secondary particle flux. These effects are clearly visible in the TDC-Scaler rates and its multiplicities, which are in anti-correlation with the pressure (one minute averaged atmospheric pressure at the HAWC site, which is measured using a barometer at the site) as shown in Figure 2.

It is important to note that the modulation of GCRs due to solar transient events are also present along with the atmospheric modulations (Arunbabu et al., 2015; Mohanty et al., 2013, 2016; Arunbabu et al., 2017; Mohanty et al., 2015) in the secondary particle flux observed by the ground-based detectors. Therefore, the accurate estimation of pressure or temperature dependence of the secondary particle rate becomes more difficult due to the presence of solar modulation along with the atmospheric modulation (Mohanty et al., 2016; Arunbabu et al., 2017). The observed pressure at the HAWC site shows a periodic variation with a period of ∼12 hrs, because of its near-equatorial location ($18^{\circ}N$). This semi-diurnal pressure variation is well known for low-latitude zones, which is associated with atmospheric tides excited by heating due to insolation absorption by ozone and water vapor (Lindzen, 1979; Carrasco et al., 2009). The TDC-scaler rates are in anti-correlation with the pressure variations and the observed TDC-scaler rates show a synchronous periodic variation with the same period as the pressure. This periodic nature observed in data sets was exploited to estimate the pressure dependence of the TDC-scaler rate.

This analysis was carried out using uninterrupted HAWC TDC-scaler system data from three different months: September, October, and November of the year 2016, to check separately for the consistency of the results and methods. The periodic anti-correlation was studied using the 'Fast Fourier Transform' (FFT) on both data sets. The FFT is an efficient and fast algorithm to compute the 'discrete Fourier transform' (DFT) and its "inverse Fourier transform" (IFT). The FFT on these data sets was performed using the TVirtualFFT routine in the ROOT framework (ROOT-website, 2015), which incorporates an FFT library FFTW (Fastest Fourier Transform in the West; Frigo and Johnson, 2005).

The FFT power spectra for the scaler rates R_1 and multiplicity rates R_{M2}, R_{M3}, R_{M4} and pressure were calculated. These data sets were passed through a high pass filter and made the DC levels of data sets close to zero, this was done to avoid the possible ripple effects in FFT if any significant gaps are present in data. Examples of the power spectra of R_1, R_{M2}, R_{M3}, R_{M4} and pressure are shown in Figure 3, respectively, from top to bottom panels. From this figure, we can clearly observe that pressure spectra has a dominant peak around two cycles per day (cpd) and the TDC-scaler rates R_1, R_{M2}, R_{M3}, R_{M4} also show a dominant peak corresponding to 2 cpd frequency. It is also visible that the power spectra of TDC-scaler rates R_1 and multiplicities R_{M2}, R_{M3}, R_{M4} show another dominant peak around 1 cpd, which corresponds to the solar diurnal anisotropy. The contribution of pressure variations on the TDC-scaler rates are significant and are clearly visible from the amplitude of the dominant peak at 2 cpd on the power spectra of pressure and TDC-scaler rates. This periodic nature observed in data sets was exploited for the accurate estimations of pressure coefficient (β_P) by segregating the non-barometric effects from the TDC-scaler rates R_1, R_{M2}, R_{M3}, and R_{M4}.

A narrow-band filter $W(f)$ as expressed in Equation 1 was used to extract the 2 cpd barometric effects from the data sets. Similar narrow-band filters were effectively used in the past to extract the atmospheric effects present in muon observations by another muon detector (Mohanty et al., 2016; Arunbabu et al., 2017). The filter expressed in the equation below is designed to select the frequencies centered at 2 cpd.

$$W(f) = \begin{cases} 1, & \text{if } |f - f_c| \leq \Delta f, \\ \sin \frac{\pi}{2} \frac{|f-f_c|}{\Delta f}, & \text{if } \Delta f < |f - f_c| \leq 2\Delta f, \\ 0, & \text{if } |f - f_c| > 2\Delta f. \end{cases} \tag{1}$$

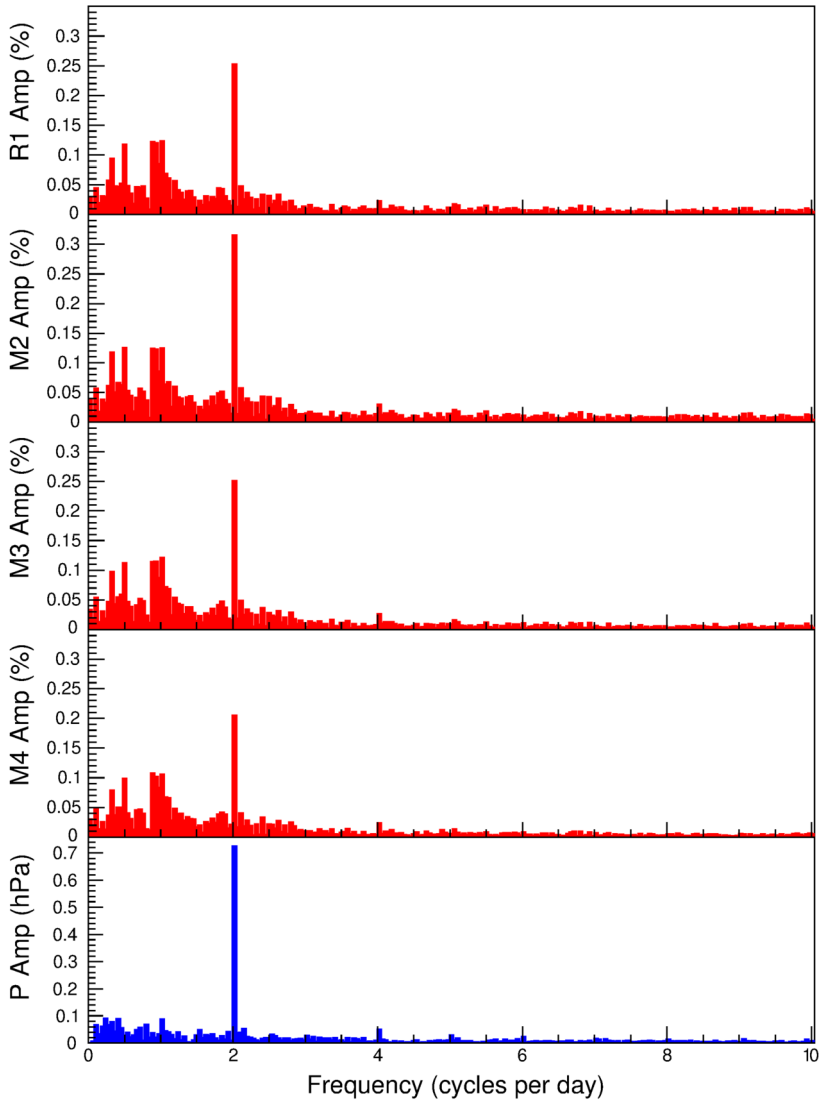

Figure 3 FFT spectrum of pressure at the bottom panel and R_1, R_{M2}, R_{M3}, and R_{M4} at top four panels, respectively, from top to bottom, for the month of October 2016.

Here f_c represents the central frequency and Δf defines the width of the filter. In this analysis, we have designed the filter with $f_c = 2$ cpd and $\Delta f = 0.05$. This designed filter has an acceptance of 100% within the frequency range from 1.95 to 2.05 cpd. The acceptance is decreasing gradually to zero following a sinusoidal behavior in both sides within the ranges of 1.95 to 1.90 cpd, and 2.05 to 2.10, respectively. The acceptance becomes zero for any frequencies outside these specified ranges. The possibility of ringing effects by the usage of filters with sharp-cut edges were avoided in this analysis by the careful design of this narrow-band filter (Harris, 1978).

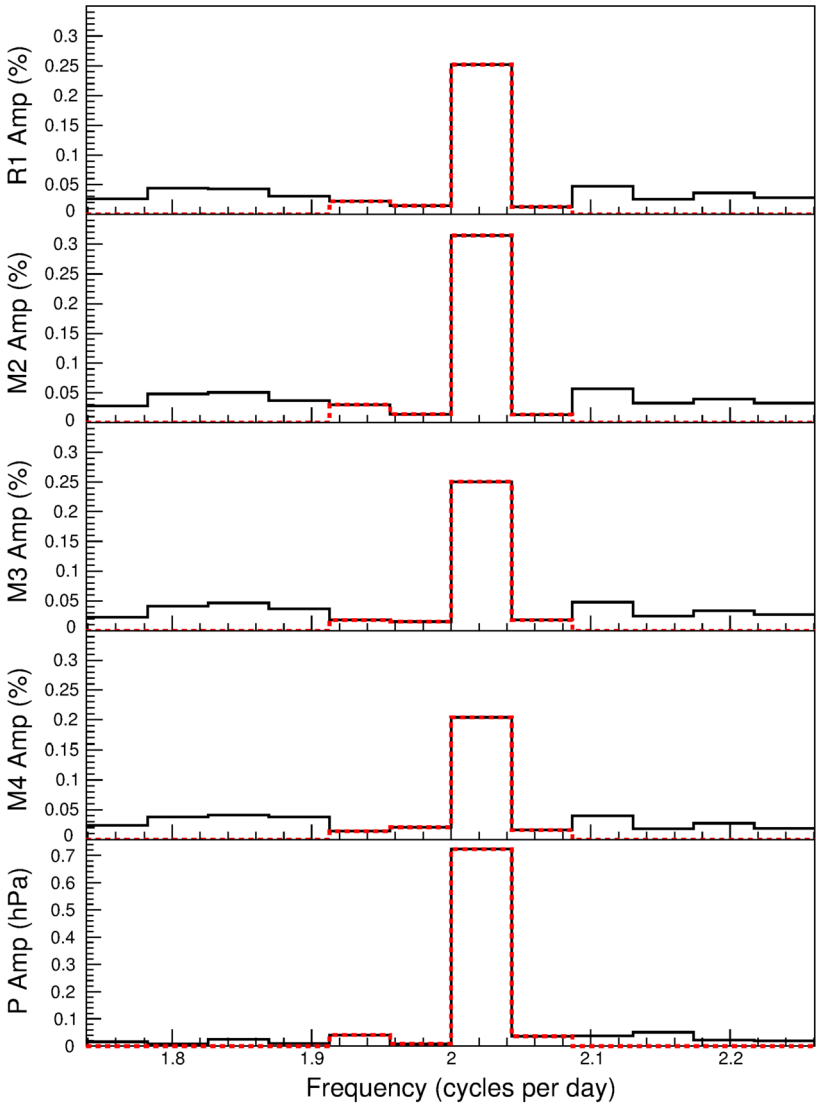

Figure 4 FFT spectrum of pressure (bottom panel) and R_1, R_{M2}, R_{M3}, and R_{M4} (top four panels, respectively, from top to bottom). Filtered spectra are shown by red dashed line and the original ones are shown by the black solid line for comparison.

The FFT frequency spectrum of the pressure and the TDC-scaler rates R_1, R_{M2}, R_{M3}, and R_{M4}, were passed through the narrow-band filter explained above. The application of this filter has extracted the desired frequencies and the resultant spectra contain only frequencies within the range from 1.90 to 2.10 cpd, which are shown in Figure 4. The initial unfiltered spectra of pressure and TDC-scaler rates (R_1, R_{M2}, R_{M3}, and R_{M4}) are shown in solid black lines, respectively, from top to bottom panels, the filtered spectra are shown in the red dashed line superimposed on them. The filtered spectrum has removed all the frequencies below

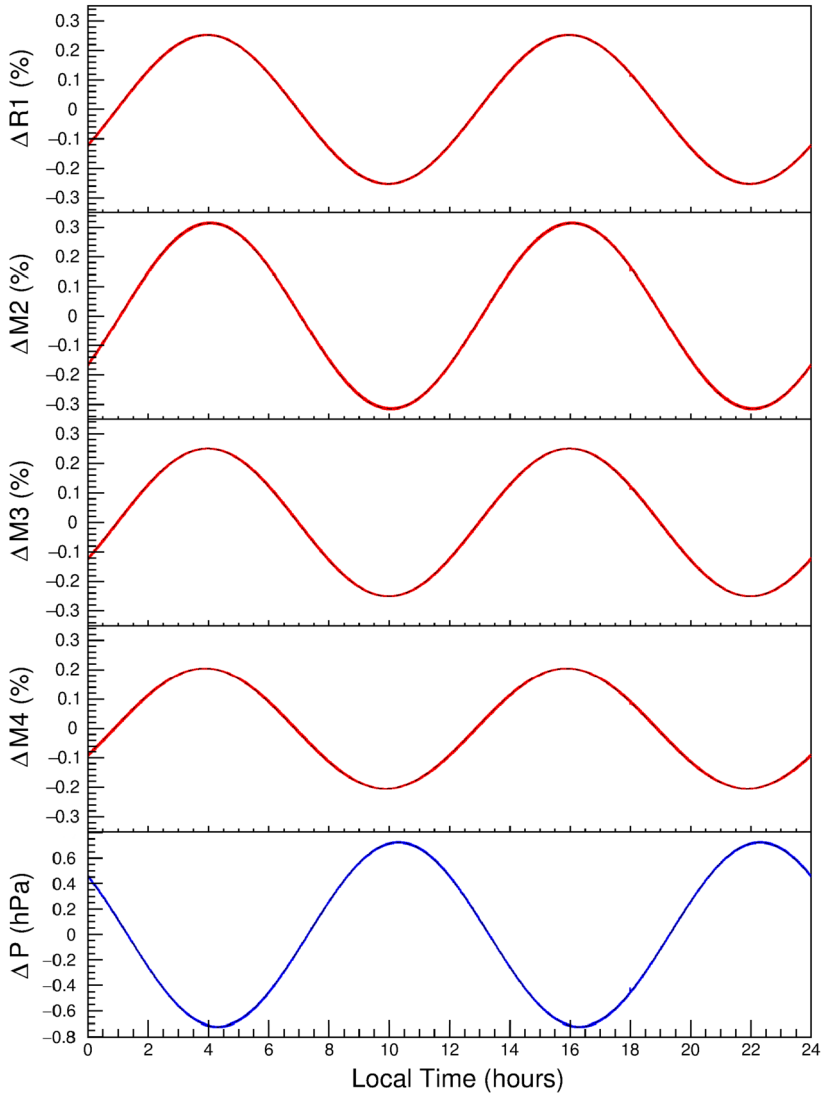

Figure 5 IFFT data of pressure and TDC-scaler rate in the local time domain, folded to a 24-hour format. The top four panels show the TDC-scaler rate R_1 and multiplicities R_{M2}, R_{M3}, R_{M4}, respectively, and the bottom one shows the pressure.

1.90 cpd and above 2.10 cpd and have a smooth sinusoidal transition on either side of f_c within the ranges of 1.95 to 1.90 cpd, and 2.05 to 2.10.

Then an inverse fast Fourier transform (IFFT) was applied on the filtered power spectra to convert them back into the time domain, as a result of the application of the filter we have extracted the 12-hour periodic component from the data sets. Figure 5 shows the filtered IFFT of these data sets, folded to fit into a 24-hour window of local time at the HAWC site (shown in the horizontal axis). From this figure, it is evident that pressure shows a 12-hour periodic nature with the maximum of the pressure occurring at approximately 10 AM and 10

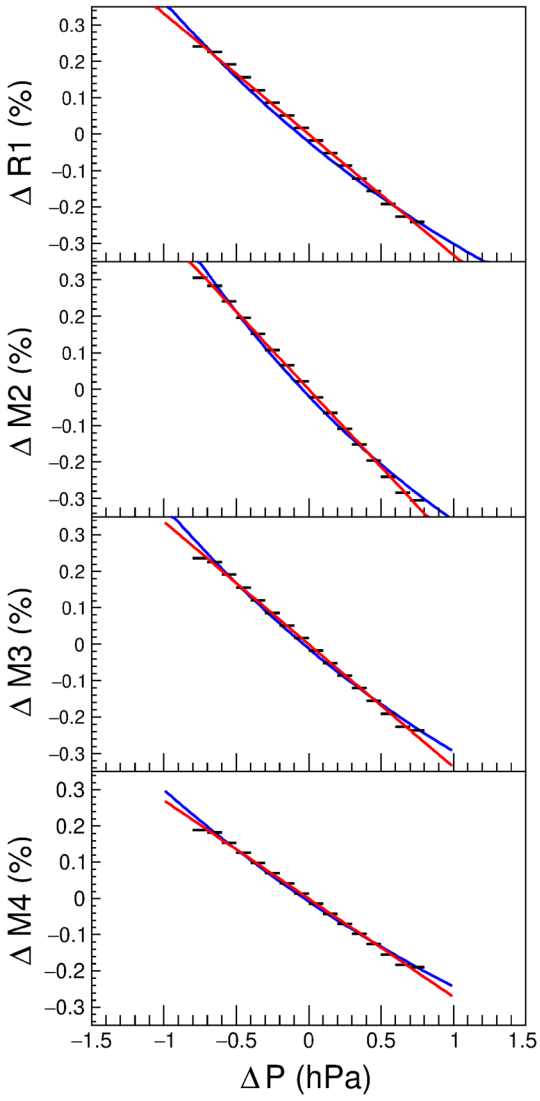

Figure 6 Dependence of TDC-scaler rates on pressure. The panels show the dependence for R_1, R_{M2}, R_{M3}, and R_{M4}, respectively, from top to bottom. The blue lines show the exponential fit and the red lines show the linear fit.

PM, whereas the minimum occurs at approximately 4 AM and 4 PM (Carrasco et al., 2009). The near perfect anti-correlation of pressure and the TDC-scaler rates R_1, R_{M2}, R_{M3}, and R_{M4} is also clearly visible in this figure, which demonstrates that the usage of the narrow-band filter has successfully isolated the effects of the 12-hour periodic nature of pressure on TDC-scaler rates from the coupled solar modulations.

The filtered IFFT of the TDC-scaler rates R_1, R_{M2}, R_{M3}, and R_{M4} plotted against the filtered IFFT of pressure are shown in Figure 6, respectively, from top to bottom. Each data point in this figure represents the mean TDC-scaler rate for a pressure bin with a width of 0.1 hPa. Empirically the dependence of TDC-scaler rates R_1 and multiplicities R_{M2}, R_{M3}, and R_{M4} on the atmospheric pressure can be approximated by an exponential function (Dorman,

Table 1 Mean value of β_P and its standard deviation σ for the months of September, October and November, 2016.

Month	Exponential		Linear	
	β_P (%/hPa)	σ	β_P (%/hPa)	σ
PMT rate R_1				
Sep.	−0.3366	0.0122	−0.3433	0.0126
Oct.	−0.3383	0.0123	−0.3430	0.0128
Nov.	−0.3358	0.0176	−0.3416	0.0183
Multiplicity R_{M2}				
Sep.	−0.4161	0.0058	−0.4304	0.0063
Oct.	−0.4117	0.0059	−0.4200	0.0061
Nov.	−0.4015	0.0060	−0.4112	0.0072
Multiplicity R_{M3}				
Sep.	−0.3203	0.0097	−0.3263	0.0105
Oct.	−0.3179	0.0091	−0.3222	0.0091
Nov.	−0.3130	0.0112	−0.3178	0.0119
Multiplicity R_{M4}				
Sep.	−0.2460	0.0091	−0.2480	0.0099
Oct.	−0.2505	0.0075	−0.2525	0.0085
Nov.	−0.2469	0.0133	−0.2507	0.0129

2004; Mohanty et al., 2016) and represented as,

$$R(P) = R(P_m) \exp^{\beta_P \Delta P}. \tag{2}$$

Here the term $R(P)$ represents the rate observed at the ground-based detectors at an atmospheric pressure P, whereas $R(P_m)$ is the observed rate at the mean pressure level. The deviation in pressure from its mean value P_m is represented by the term ΔP and the pressure coefficient is represented as β_P. From Figures 4 and 5 it is evident that the amplitude of pressure variation is small and of the order of ~ 0.7 hPa. Since the typical value of β_P is much less than one (Mohanty et al., 2016) and the numerical value of ΔP is < 1 we can ignore the higher-order terms in the Taylor series expansion of the exponential function in Equation 2 and can consider only the first-order term, hence make a linear approximation,

$$R(P) = R(P_m)\ \ (1 + \beta_P \Delta P). \tag{3}$$

In our analysis we consider both exponential and linear approximation approaches because the HAWC site can experience stormy weather by virtue of its geographical location, which can cause significant variations in pressure. We use both methods to cross-check the consistency even with a pressure amplitude ~ 0.7 hPa. The Figure 6 represents the dependence of TDC-scaler rates R_1, R_{M2}, R_{M3}, and R_{M4} on the atmospheric pressure. The blue lines show a fit of an exponential function '$C_1 + \exp^{\beta_P \Delta P}$' and the red lines show the fit of the linear approximation '$C_2 + \beta_P \Delta P$'.

Similar analyses were carried out for the TDC-scaler rates of all the 1180 PMTs and 295 WCDs. The β_P were estimated for the R_1 rates corresponding to 1180 PMTs and the R_{M2},

Table 2 Mean value of β_P for the multiplicities.

Multiplicity	Median rigidity GV	β_P (%/hPa) (exponential)	β_P (%/hPa) (linear)
R1	41.97	−0.337	−0.343
M2	41.46	−0.401	−0.420
M3	42.28	−0.317	−0.322
M4	45.04	−0.248	−0.250

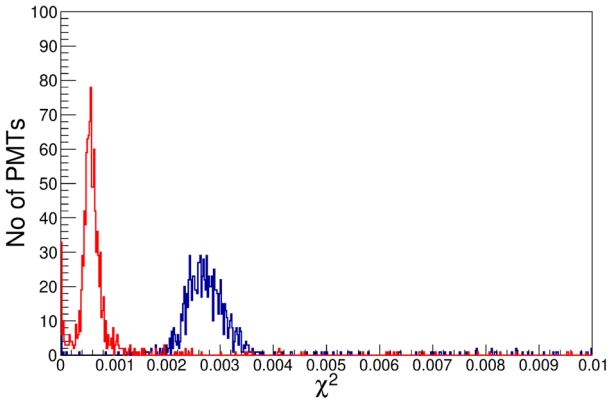

Figure 7 χ^2 of both fitting methods for all the PMTs (R_1) are shown in the figure. The red distribution is for the linear method and the blue one is for the exponential method.

R_{M3}, and R_{M4} rates corresponding to the 295 WCDs. Data from the months of September, October, and November in 2016 were used in this analysis. The β_P were estimated using both exponential and linear approximation approaches, and the distribution of β_P for the TDC-scaler rate R_1 during the three months are shown in Figure 14. The mean value of β_P and its standard deviation σ for R_1, R_{M2}, R_{M3}, and R_{M4} for each month is given in the Table 1. The efficiency corrected TDC-scaler rates of HAWC is having a statistical accuracy $< 0.01\%$ and the estimated β_P for the three months are compatible within this statistical uncertainty, therefore, the corrections applied will not make significant change in the accuracy of TDC-scaler rates.

The pressure modulation observed is a purely physical phenomenon (due to the atmospheric properties) and therefore, the effects of pressure modulation are independent of the detector. We took advantage of this fact and used the deviations of β_P for a PMT/WCD from the mean value as a measure to quantify the health of a PMT/WCD and isolate the bad-ones from our further analysis (Detailed explanation of this selection process is given in Appendix B).

5. Pressure Correction

Table 2 shows the mean value of β_P for TDC-scaler rates estimated using both exponential and linear methods for the months of September, October, and November 2016. Whereas the correspondent distributions of the χ^2 for R_1 are shown in Figure 7, The mean value of χ^2 for R_1 and the multiplicities (R_{M2}, R_{M3} and R_{M4}) computed using both exponential and linear methods are given in Table 3. From Figure 7 and Table 3, it is clear that the linear

Table 3 Mean χ^2 value for exponential and linear fitting.

Multiplicity	Mean χ^2 (exponential)	Mean χ^2 (linear)
R1	2.7×10^{-3}	5.7×10^{-4}
M2	5.1×10^{-3}	7.1×10^{-4}
M3	2.4×10^{-3}	6.8×10^{-4}
M4	1.4×10^{-3}	5.5×10^{-4}

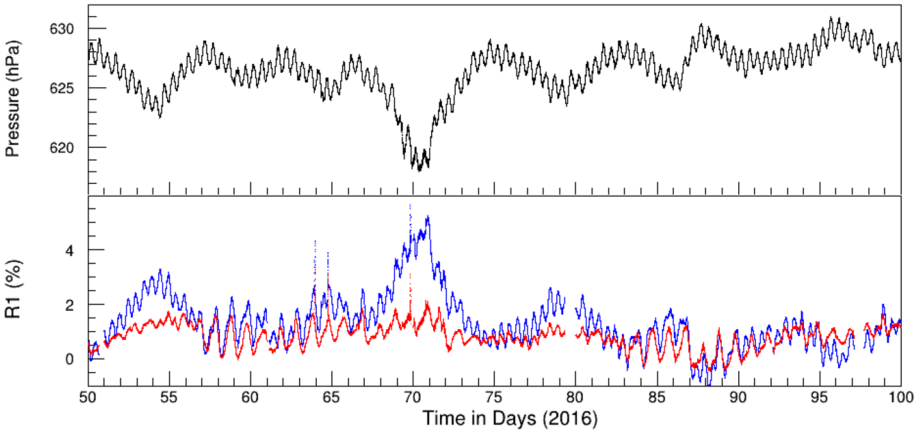

Figure 8 Top panel shows the pressure observed at the HAWC site and bottom panel shows the percentage variation of efficiency corrected combined $R1$, the blue curve is before correction and the red one after pressure correction.

method have the least χ^2 in comparison with the exponential method. It has to be noted that for both methods the estimated β_P values are consistent within the statistical accuracy of the experiment. Since the best fit was obtained using the linear method with lower χ^2, we are going to use this method for the pressure correction of the HAWC TDC-scaler system.

The pressure correction was applied to the rates R_1 using the mean β_P and in order to show the improvement, the efficiency corrected combined rates R_1 before and after pressure correction are shown in Figure 8. For a comparison the pressure observed at the HAWC site is also shown in this figure. From this we can see how effectively the method has removed the pressure modulations. Moreover, the FFT was applied to the R_1 of the year 2016 before and after pressure corrections the resultant power spectra are shown in Figure 9 in which the top panel shows the power spectra after pressure correction and the bottom one shows the same before pressure correction. From this figure we can clearly observe that the amplitude of 2 cpd which was mainly due to the pressure component was reduced drastically, whereas the amplitudes corresponding to 1 cpd have slightly increased due to the solar diurnal anisotropy. This diurnal anisotropy component was masked by the pressure modulations and the exact measurement of its amplitude is only possible after the pressure correction. A slight peak in amplitude at the 2 cpd can be observed and may be due to the second harmonic of the solar diurnal anisotropy, the higher harmonics were also observed in other experiments and the amplitude of this second harmonic is comparable with the same found in earlier studies (Mohanty et al., 2015). Finally, the multiplicities R_{M2}, R_{M3} and R_{M4} were

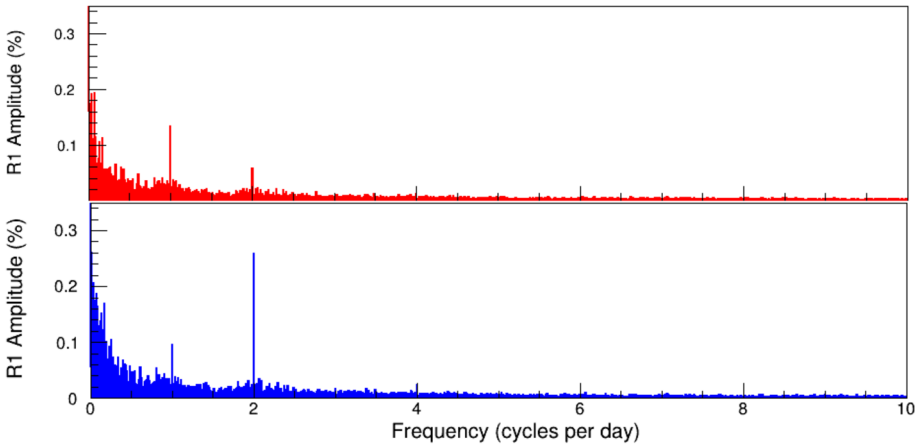

Figure 9 The power spectrum of $R1$ for the year 2016, the bottom panel shows the power spectrum before pressure correction in blue, and the top panel shows the same after applying pressure correction in red.

also made suitable for solar modulation studies by performing the pressure correction in a similar method using the corresponding β_P estimated, which are shown in Table 2.

6. Discussion

The efficiency corrected combined HAWC TDC-scaler rates have high statistical accuracy and can measure any variation in GCR rate larger than 0.01%. The observed TDC-scaler have complex nature because it contains both solar and atmospheric modulations. Therefore, the measured rates of HAWC TDC-scaler system are well-suited for studies of solar modulations and space weather if the atmospheric modulations are filtered out. After the atmospheric corrections, the solar modulations present in the data will have the $\sim$1-day periodic behavior known as the solar diurnal anisotropy along with FDs and the periodic modulations due to the solar rotation and 11 year solar cycle. Although, since both solar and pressure modulations are present in the observed data, it is difficult to make the atmospheric pressure corrections using the conventional method of taking the direct correlation between the rate and pressure (Mohanty et al., 2016; Arunbabu et al., 2017), an illustration of this is given in Appendix A. The usage of a coupled regression method is also ruled out since the dependence on the solar wind parameters of the GCR intensity is not well studied and we are unaware of whether it is a linear or non-linear dependence because both approaches have been used in various studies of GCR diffusion in a turbulent magnetic field (Potgieter et al., 2014; Giacalone and Jokipii, 1999; Candia and Roulet, 2004; Matthaeus et al., 2003; Shalchi, 2010).

We have made use of the periodic behavior of the pressure to extract the pressure dependence from the data using the FFT method, which is well suited to the atmospheric corrections in the TDC-scaler rate (Mohanty et al., 2016; Arunbabu et al., 2017). This method was successfully applied to estimate the β_P for the months of September, October and November in 2016. The analysis provided a consistent value for β_P using both the exponential and linear approximations, and the values are given in Table 1.

The estimated mean β_P for the TDC-scaler rates and multiplicities using both exponential and linear methods are given in Table 2. These values were fairly consistent with each

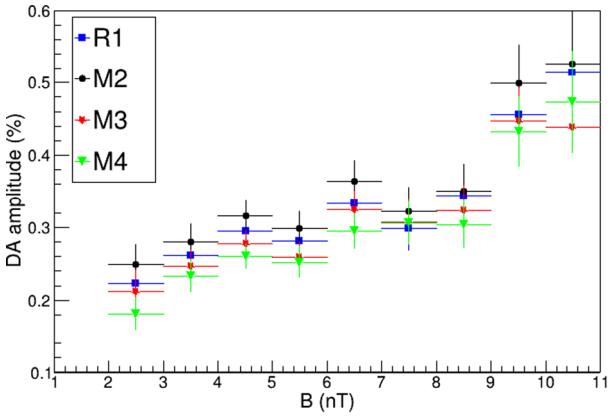

Figure 10 Relationship between the diurnal anisotropy amplitude and the total interplanetary magnetic field of the solar wind.

other within the statistical accuracy of the one minute averaged measurement of the experimental setup. The vertical cut-off rigidity of the HAWC TDC-scaler system is 7.9 GV (Lara, 2013), and its median rigidity for the multiplicities varies within the range of $\sim 41-45$ GV. Because of their short lifetime most of the pions and kaons that are produced by primaries of this energy range will decay well before reaching the detector level.

The estimated β_P is different for each multiplicity, showing a dependency on the median energy of the observation as shown in Table 2. We are aware that the variation of β_P depend also on multiple other factors, such as mean viewing direction (zenith angle of incident particle flux), the primary particles and the secondary particles detected (Dorman, 2004; Chilingarian and Karapetyan, 2011). For instance, the rate R_1 is dominated by the secondary electromagnetic particles (Abeysekara, 2012). The β_P should have an inverse proportionality to the viewing direction (Chilingarian and Karapetyan, 2011). It should be noted that the mini neutron monitor which detects mainly neutrons, has a pressure coefficient almost double of that obtained by HAWC (Lara, Borgazzi, and Caballero-Lopez, 2016).

We have removed the abnormally behaving PMTs in the case of $R1$ and the associated WCDs in the case of multiplicities before combining/averaging the TDC-scaler data. Pressure corrections were applied using the corresponding β_P. These corrections have drastically removed the dominant pressure modulation in the power spectrum, they also improved the measurement of diurnal anisotropy component, which is clear from Figure 8. Selection of properly behaving PMTs using β_P has improved the accuracy of data and made it much more suitable to measure even small variations due to solar modulation.

The HAWC TDC-scaler data after efficiency and pressure corrections are well suited for short-period solar modulation studies such as solar diurnal modulation, FDs, 27-day variations due to rotation, and variation due to high-speed streamers. The efficiency and pressure corrected combined data have a statistical accuracy of $< 0.01\%$ for every minute.

6.1. Diurnal Anisotropy

The solar diurnal anisotropy is the resultant of solar wind drift and diffusion, resulting in a periodic variation of GCR intensity at Earth (Mohanty et al., 2016). As one can observe in Figure 9 the diurnal anisotropy and its first harmonics are dominantly present in the corrected HAWC TDC-scaler data. We have applied a high pass filter (> 0.9 cpd) which removes all the slow variations from the data such as Forbush decreases and passes through the fast variation with frequency greater than 0.9 cpd. The application of this filter mainly retain

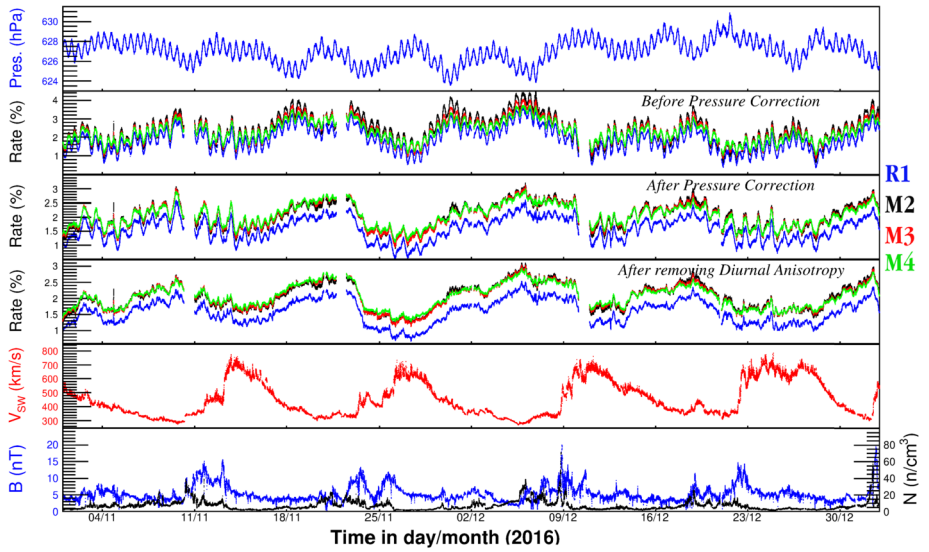

Figure 11 Data shown in this figure are for the months of November and December of 2016. The first panel shows the pressure measured at HAWC site, the second, third and fourth panels show the percentage deviations of HAWC TDC-scaler rates before pressure correction, after pressure corrections and after removing diurnal anisotropy, respectively. It should be noted that the vertical axis ranges are chosen to show the variations clearly. The fifth panel shows the solar wind velocity (V_{sw}) and the last panel shows the total magnetic field (B) and particle density (N) of the solar wind obtained from OMNI data base (https://omniweb.gsfc.nasa.gov/ow.html).

the solar diurnal anisotropy (with 1 cpd periodicity) and its harmonics (with 2 cpd periodicity). Using this high pass filtered data we estimated the amplitude of diurnal anisotropy for every day and compared it with the daily average solar wind magnetic field, which is shown in Figure 10. We can see an evident relation between the observed diurnal anisotropy amplitude and the solar wind magnetic field (with a bin size of 1 nT) during quiet time periods. This relation is attributed to the diffusion process of GCRs in the ambient solar wind, resulting in a powerful tool to explore the large scale magnetic field structures related to the space weather. More detailed analysis of this will be presented in future work.

6.2. Short-Term Modulation

We are aware that the total atmospheric correction will be completed only if we correct the data for temperature effects known as 'seasonal variations'. But HAWC is located closer to the equator with latitude 18°59′41″ N, at these latitudes the temperature variation of atmospheric column above the experiment will be minimal. Even though the ground temperature varies largely, higher atmospheric temperature remains stable for time scales of seasons (Arunbabu et al., 2017). Therefore for short-term solar modulation like FDs, and studies of space weather transient the temperature corrections can be neglected.

The study of FDs and other short-term solar modulation can be carried out after removing solar diurnal anisotropy, for which we used a band rejection filter which removes the periodic diurnal component and its first harmonics from the data (Mohanty et al., 2016). As an example of the HAWC TDC-scaler data for solar modulation studies, we present Figure 11. For a comparison HAWC TDC-scaler rate before pressure correction, after pressure correction and after removal of diurnal anisotropy are shown in panels 2, 3 and 4, respectively, in

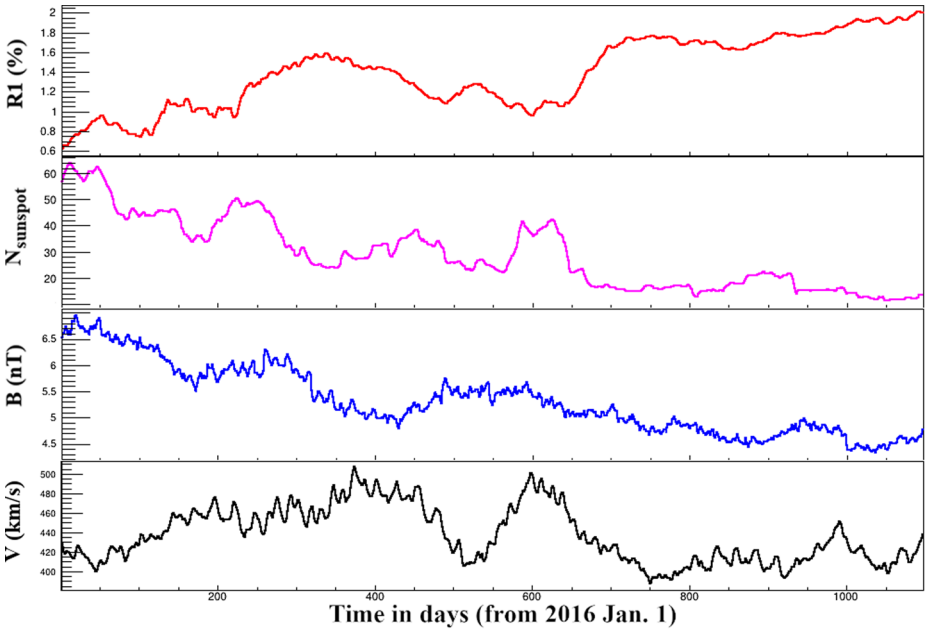

Figure 12 Top panel shows the HAWC TDC-scaler rate R1 for three years from 2016 to 2018. Second panel shows the sunspot number, whereas third and fourth panels show the magnetic field and velocity of solar wind, respectively.

this figure, which shows how effectively pressure modulations were removed and the data made suitable for solar modulation studies. From this figure, we can see a clear correlation of TDC-scaler rates with the solar wind velocity. We are doing a more detailed analysis of the dependency of solar wind parameters on the GCR flux observed at Earth using a wider range of data sets. A detailed explanation of these studies are out of the scope of this paper and will be explained in future articles using HAWC data, but it is worth mentioning here the observation of an interplanetary flux-rope by HAWC (Akiyama et al., 2020).

6.3. Long-Term Modulations

Long-term solar modulations have been well known for decades (Potgieter, 2013), to study this we have used a 60-day running average filter. This filter has removed all the short-term modulations in the HAWC TDC-scaler rate. The same filter is also used for the sunspot number and the solar wind velocity and magnetic field. We have analyzed the data for three years starting from 1 January 2016 to 31 December 2018, which are shown in Figure 12. From this, we can see a dependence of the observed rate on the interplanetary magnetic field and solar wind velocity. The well-known anti-correlation with the sunspot number is also visible in this figure. Even though the seasonal variation can be smaller for HAWC due to its location, but considering the statistical accuracy of measurement the instrument is capable of it is necessary to perform this correction. Our future work aims to study this atmospheric modulation and corrections, that will make the HAWC data ready for long-term modulations.

7. Summary

Large area GCR detectors like HAWC can measure the secondary flux with high accuracy and therefore, the solar modulation of GCRs observed by this kind of ground-based detectors is a good tool for the identification of space-weather transient events and study their geo-effectiveness and predictions. Although, since atmospheric modulations are present along with solar modulations in the ground-based GCR observations, it is necessary to have an accurate estimation of the pressure coefficient β_P and perform efficient corrections to remove the pressure induced modulations from the data to make it suitable for studying the solar-induced phenomena. Due to its latitudinal location close to the equator, the HAWC site has a prominent 12-hour periodic nature in pressure variations and the strong anti-correlation between the pressure and the TDC-scaler rate is extracted by exploiting this periodic nature. Specifically, we use the FFT and a narrow-band filter to effectively isolate the pressure induced modulations from the solar modulations. The anti-correlation observed after applying this method was made possible by accurate estimation of β_P. The reliability and accuracy of this method were proven by the consistent results obtained for the months of September, October and November in 2016. As a side benefit of this method and since the pressure modulation were proven a physical phenomenon, the deviations of β_P of a PMT from the mean value is considered as a quantitative measure of the health of the PMT and its normal behavior, helping in this way to locate the PMTs behaving abnormally and remove them from the combined HAWC TDC-scaler data.

The efficiency and pressure corrected HAWC TDC-scaler data is suitable for solar modulation and space-weather studies, any variation $> 0.01\%$ can be effectively measured using this large area detector. Having a relatively low cut-off rigidity and high sensitivity HAWC can study the solar modulations that are sensitive to weak interplanetary structures and solar wind parameters. To show this sensitivity we presented preliminary results of the diurnal anisotropy and short- and long-term solar modulation as seen by the correlation between the TDC-scaler rates and the solar wind velocity and magnetic field.

Appendix A: Comparison of FFT Method with Conventional Method

The application of the FFT filter on the TDC-scaler rate has effectively isolated the pressure modulation from the coupled solar modulation in the TDC-scaler rate, allowing a more accurate measurement of β_P. In this appendix, we demonstrate the effectiveness of this method over the conventional method. Figure 13 shows both the conventional method and the FFT filter method, the fitting of a linear function is most suitable, and the fit quality is better for the FFT method. The estimated β_P during three months of observation using both methods are given in Table 4, from these values we can see how consistent and effective is the FFT method for estimating β_P. Using the conventional method, the estimated β_P values are not consistent, the deviation is much higher than the required accuracy of HAWC TDC-scaler system, whereas the FFT method estimated the β_P with an accuracy within the required limits. The variation of β_P using the conventional method is due to the presence of solar modulation, this method was not able to decouple the solar modulation from the atmospheric one.

Appendix B: Checking the Health of PMTs Using β_P

Once the pressure modulations were isolated and the pressure coefficient β_P was estimated for all 1180 PMTs, we take advantage of the fact that this modulation is a purely physical

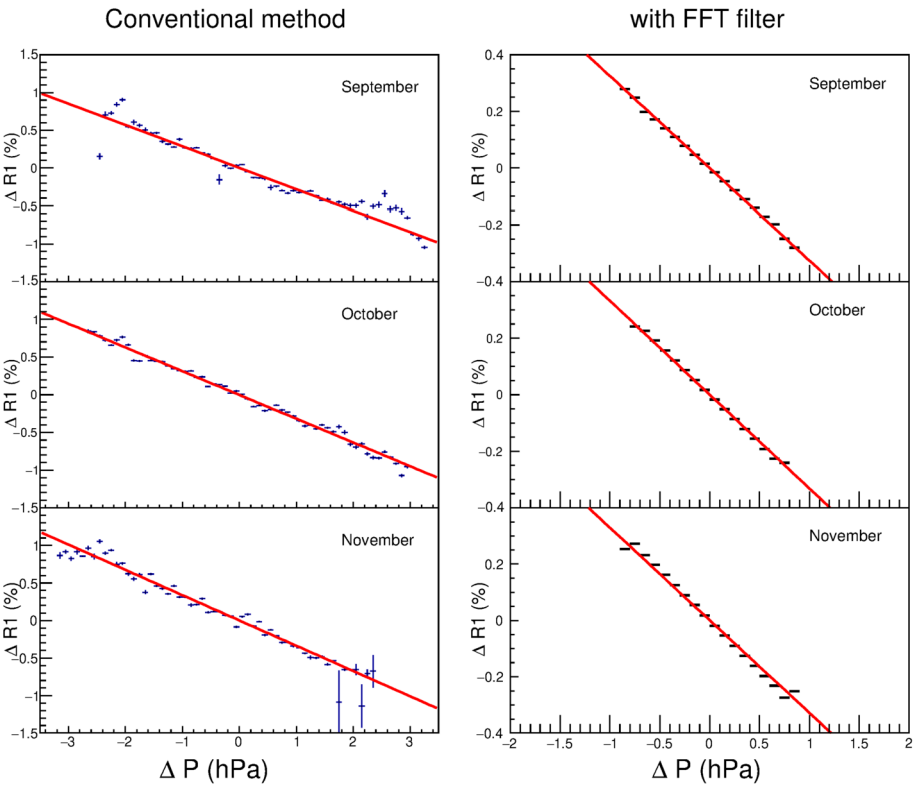

Figure 13 The rows from top to bottom show data of months of September, October, and November in the corresponding order. The first column shows the dependency of TDC-scaler rate on pressure difference using the conventional method. The second column shows the same with the FFT filter method.

Table 4 β_P estimated using different methods.

Month	β_P from conventional method	β_P from with FFT filter
September	−0.2824	−0.3396
October	−0.3153	−0.3417
November	−0.3368	−0.3373

phenomenon (due to the atmospheric properties) and therefore, the effects of pressure modulation are independent of the detector. This means that the obtained β_P should be similar for the 1180 PMT and the deviation of β_P from its mean value of a particular PMT/WCD is due to malfunction of that particular PMT or its associated components.

The distribution of β_P $(R1)$ of all 1180 PMTs for the months of September, October, and November of 2016 is shown in Figure 14, which is Gaussian in nature. A Gaussian fit to this distribution gives us a standard deviation as shown in Table 1. We chose a cut-off limit of 2 and 3σ levels. Using this criterion we have classified the PMTs and WCD s, which are shown in Table 5.

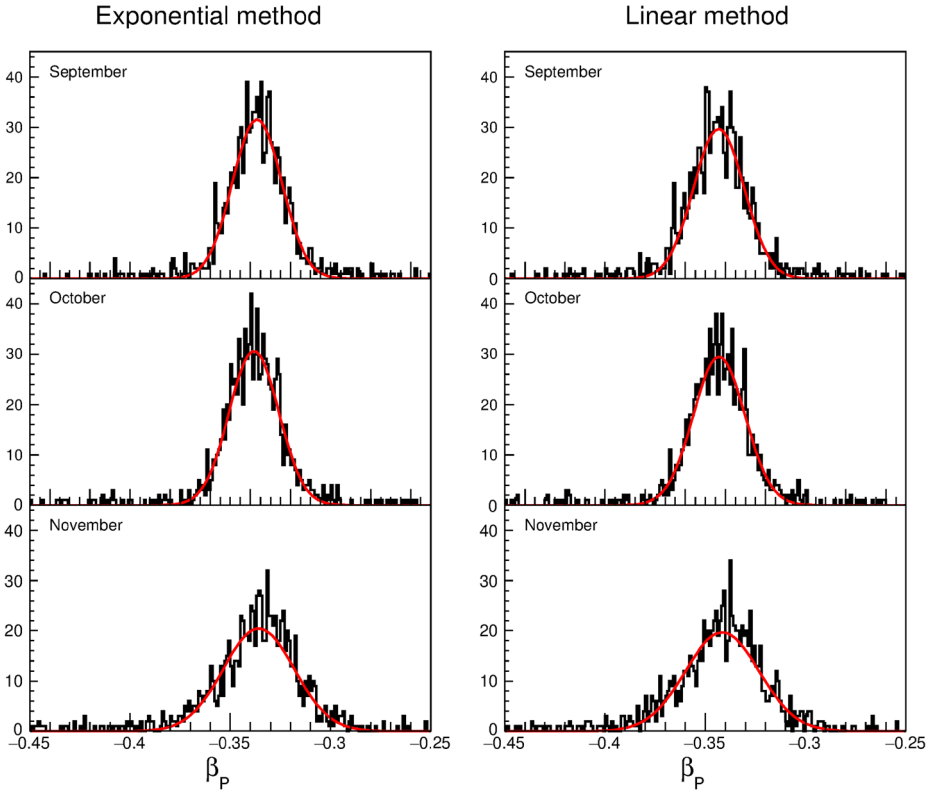

Figure 14 The distributions of the pressure coefficient β_P of all PMTs ($R1$) for the months of September (top), October (middle), and November (bottom), 2016 are shown. The first column shows the distribution obtained using the exponential method and the second column shows that by linear method. The red lines show the Gaussian fit for these distributions.

Table 5 Classification of PMTs and WCDs. Third row gives the number of PMTs/WCDs that are good, fourth row gives the number of PMTs/WCDs with in $3-5\sigma$ range, fifth one shows that above 5σ, and the last one shows that with no data. Column 2,3 and 4 correspond to single PMT rates R1, column 5, 6 and 7 to Multiplicity M2, column 8, 9, 10 for Multiplicity M3, and column 11, 12 and 13 to Multiplicity M4.

Month	PMT (R1)			Multiplicity M2			Multiplicity M3			Multiplicity M4		
	Sep	Oct	Nov	Sep	Oct	Nov	Sep	Oct	Nov	Sep	Oct	Nov
Good	1027	1005	999	260	245	226	266	255	263	256	240	250
3σ to 5σ	40	24	40	15	11	9	4	7	8	8	9	8
Above 5σ	103	142	128	18	38	58	23	32	22	24	37	29
No-data	10	9	13	2	1	2	2	1	2	7	9	8

The value of β_P and its deviation from the mean value are the quantitative measure of the health of a PMT. These give us a measure of how well a PMT is functioning within its normal gain mode. Considering this criterion we isolated the PMTs and WCDs outside this 3σ range, and included PMTs and WCDs within 3σ range for our further analysis of solar modulations. This selection process improved the accuracy of the measurement and

reduced the systematic errors. This process has made the data more suitable for accurate solar modulation studies.

Acknowledgements We acknowledge use of NASA/GSFC's Space Physics Data Facility's OMNIWeb (or CDAWeb or ftp) service, and OMNI data. The author Arunbabu acknowledges financial support from 'DGAPA-UNAM'. We acknowledge the support from: the US National Science Foundation (NSF); the US Department of Energy Office of High-Energy Physics; the Laboratory Directed Research and Development (LDRD) program of Los Alamos National Laboratory; Consejo Nacional de Ciencia y Tecnología (CONACyT), México, grants 271051, 232656, 260378, 179588, 254964, 258865, 243290, 132197, A1-S-46288, A1-S-22784, cátedras 873, 1563, 341, 323, Red HAWC, México; DGAPA-UNAM grants IG101320, IN111315, IN111716-3, IN111419, IA102019, IN110621, IN110521; VIEP-BUAP; PIFI 2012, 2013, PROFOCIE 2014, 2015; the University of Wisconsin Alumni Research Foundation; the Institute of Geophysics, Planetary Physics, and Signatures at Los Alamos National Laboratory; Polish Science Centre grant DEC-2018/31/B/ST9/01069, DEC-2017/27/B/ST9/02272; Coordinación de la Investigación Científica de la Universidad Michoacana; Royal Society – Newton Advanced Fellowship 180385; Generalitat Valenciana, grant CIDEGENT/2018/034; Chulalongkorn University's CUniverse (CUAASC) grant; Coordinación General Académica e Innovación (CGAI-UdeG), PRODEP-SEP UDG-CA-499. Thanks to Scott Delay, Luciano Díaz and Eduardo Murrieta for technical support.

Declarations

Disclosure of Potential Conflicts of Interest The authors declare that they have no conflicts of interest.

References

Abeysekara, A.U. HAWC Collaboration: 2012, On the sensitivity of the HAWC observatory to gamma-ray bursts. *Astropart. Phys.* **35**, 641. DOI.

Abeysekara, A.U., Alfaro, R., Alvarez, C., Álvarez, J.D., Arceo, R., Arteaga-Velázquez, J.C., et al.: 2018, Data acquisition architecture and online processing system for the HAWC gamma-ray observatory. *Nucl. Instrum. Methods Phys. Res., Sect. A, Accel. Spectrom. Detect. Assoc. Equip.* **888**, 138. DOI.

Achard, P., Adriani, O., Aguilar-Benitez, M., van den Akker, M., Alcaraz, J., Alemanni, G., et al.: 2004, Measurement of the atmospheric muon spectrum from 20 to 3000 GeV. *Phys. Lett. B* **598**, 15. DOI.

Agostinelli, S., Allison, J., Amako, K., Apostolakis, J., et al.: 2003, GEANT4—a simulation toolkit. *Nucl. Instrum. Methods Phys. Res., Sect. A, Accel. Spectrom. Detect. Assoc. Equip.* **506**, 250. DOI.

Akiyama, S., Alfaro, R., Alvarez, C., Angeles Camacho, J.R., Arteaga-Velázquez, J.C., Arunbabu, K.P., et al.: 2020, Interplanetary magnetic flux rope observed at ground level by HAWC. *Astrophys. J.* **905**, 73. DOI.

Arunbabu, K.P., Lara, A., Ryan, J., HAWC Collaboration: 2019, Atmospheric pressure dependance of HAWC scaler system. In: *36th International Cosmic Ray Conference (ICRC2019)* **36**, 1095.

Arunbabu, K.P., Antia, H.M., Dugad, S.R., Gupta, S.K., Hayashi, Y., Kawakami, S., et al.: 2013, High-rigidity Forbush decreases: due to CMEs or shocks? *Astron. Astrophys.* **555**, A139. DOI.

Arunbabu, K.P., Antia, H.M., Dugad, S.R., Gupta, S.K., Hayashi, Y., Kawakami, S., et al.: 2015, How are Forbush decreases related to interplanetary magnetic field enhancements? *Astron. Astrophys.* **580**, A41. DOI.

Arunbabu, K.P., Ahmad, S., Chandra, A., Dugad, S.R., Gupta, S.K., Hariharan, B., et al.: 2017, Dependence of the muon intensity on the atmospheric temperature measured by the GRAPES-3 experiment. *Astropart. Phys.* **94**, 22. DOI.

Asorey, H., Núñez, L.A., Suárez-Durán, M.: 2018, Preliminary results from the Latin American Giant Observatory space weather simulation chain. *Space Weather* **16**, 461. DOI.

Burlaga, L.F., McDonald, F.B., Goldstein, M.L., Lazarus, A.J.: 1985, Cosmic ray modulation and turbulent interaction regions near 11 Au. *J. Geophys. Res.* **90**, 12027. DOI.

Candia, J., Roulet, E.: 2004, Diffusion and drift of cosmic rays in highly turbulent magnetic fields. *J. Cosmol. Astropart. Phys.* **10**, 007. DOI.

Carrasco, E., Carramiñana, A., Avila, R., Gutiérrez, C., Avilés, J.L., Reyes, J., et al.: 2009, Weather at Sierra Negra: 7.3-yr statistics and a new method to estimate the temporal fraction of cloud cover. *Mon. Not. Roy. Astron. Soc.* **398**, 407. DOI.

Chilingarian, A., Karapetyan, T.: 2011, Calculation of the barometric coefficients at the start of the 24th solar activity cycle for particle detectors of Aragats Space Environmental Center. *Adv. Space Res.* **47**, 1140. DOI.
Dorman, L.I.: 2004, *Cosmic Rays in the Earth's Atmosphere and Underground* **303**, Kluwer Academic, Dordrecht. DOI.
Enriquez-Rivera, O., Lara, A., Caballero-Lopez, R.: 2015, Solar event simulations using the HAWC scaler system. In: *34th International Cosmic Ray Conference (ICRC2015)* **34**, 226.
Forbush, S.E.: 1954, World-wide cosmic-ray variations, 1937-1952. *J. Geophys. Res.* **59**, 525. DOI.
Frigo, M., Johnson, S.G.: 2005, The design and implementation of FFTW3. *Proc. IEEE* **93**, 216.
Giacalone, J., Jokipii, J.R.: 1999, The transport of cosmic rays across a turbulent magnetic field. *Astrophys. J.* **520**, 204. DOI.
Greisen, K.: 1960, Cosmic ray showers. *Annu. Rev. Nucl. Part. Sci.* **10**, 63. DOI.
Grieder, P.K.F.: 2001, *Cosmic Rays at Earth*, Elsevier, Amsterdam.
Harris, F.J.: 1978, On the use of windows for harmonic analysis with the discrete Fourier transform. *Proc. IEEE* **66**, 51.
Heck, D., Knapp, J., Capdevielle, J.N., Schatz, G., Thouw, T.: 1998, CORSIKA: a Monte Carlo code to simulate extensive air showers 6019, TIB Hannover, Hannover.
Jara Jimenez, A.R., Lara, A., Arunbabu, K.P., Ryan, J., HAWC Collaboration: 2019, Effects of the atmospheric electric field on the HAWC scaler rate. In: *36th International Cosmic Ray Conference (ICRC2019)* **36**, 1087.
Kudela, K., Storini, M., Hofer, M.Y., Belov, A.: 2000, Cosmic rays in relation to space weather. *Space Sci. Rev.* **93**, 153. DOI.
Lara, A.: 2013, HAWC sensitivity to solar events. In: *33rd International Cosmic Ray Conference* **33**, 1464.
Lara, A., Borgazzi, A., Caballero-Lopez, R.: 2016, Altitude survey of the galactic cosmic ray flux with a Mini Neutron Monitor. *Adv. Space Res.* **58**, 1441. DOI.
Lindzen, R.S.: 1979, Atmospheric tides. *Annu. Rev. Earth Planet. Sci.* **7**, 199. DOI.
Matthaeus, W.H., Qin, G., Bieber, J.W., Zank, G.P.: 2003, Nonlinear collisionless perpendicular diffusion of charged particles. *Astrophys. J.* **590**, L53. DOI.
Mohanty, P.K., Atri, D., Dugad, S.R., Gupta, S.K., Hariharan, B., Hayashi, Y., et al.: 2013, Solar diurnal anisotropy measured using muons in GRAPES-3 experiment in 2006. *Pramana* **81**, 343. DOI.
Mohanty, P.K., Antia, H.M., Arunbabu, K.P., Dugad, S., Gupta, S.K., Balakrishnan, H.H., et al.: 2015, Measurements of solar diurnal ansiotropy with GRAPES-3 experiment. In: *34th International Cosmic Ray Conference (ICRC2015)*, **34**, 42.
Mohanty, P.K., Ahmad, S., Antia, H.M., Arunbabu, K.P., Chandra, A., Dugad, S.R., et al.: 2016, Fast Fourier transform to measure pressure coefficient of muons in the GRAPES-3 experiment. *Astropart. Phys.* **79**, 23. DOI.
Mohanty, P.K., Arunbabu, K.P., Aziz, T., Dugad, S.R., Gupta, S.K., Hariharan, B., et al.: 2016, Transient weakening of Earth's magnetic shield probed by a cosmic ray burst. *Phys. Rev. Lett.* **117**, 171101. DOI.
Mohanty, P.K., Ahmad, S., Arunbabu, K.P., Chandra, A., Dugad, S.R., et al.: 2017, Long-term correction of GRAPES-3 muon telescope efficiency. In: *35th International Cosmic Ray Conference (ICRC2017)*, **35**, 357
Nakamura, K., et al. (Particle Data Group): 2010, Review of particle physics. *J. Phys. G, Nucl. Part. Phys.* **37**, 075021.
Olive, K.A., Particle Data Group: 2014, Review of particle physics. *Chin. Phys. C* **38**, 090001. DOI.
Potgieter, M.S.: 2013, Solar modulation of cosmic rays. *Living Rev. Solar Phys.* **10**, 3. DOI.
Potgieter, M.S., Vos, E.E., Boezio, M., De Simone, N., Di Felice, V., Formato, V.: 2014, Modulation of galactic protons in the heliosphere during the unusual solar minimum of 2006 to 2009. *Solar Phys.* **289**, 391. DOI.
Richardson, I.G., Cane, H.V., Cliver, E.W.: 2002, Sources of geomagnetic activity during nearly three solar cycles (1972-2000). *J. Geophys. Res.* **107**(A8), 1187. DOI.
Shalchi, A.: 2010, A unified particle diffusion theory for crossfield scattering: subdiffusion, recovery of diffusion, and diffusion in three-dimensional turbulence. *Astrophys. J.* **720**, L127. DOI.
Smart, D.F., Shea, M.A.: 2005, A review of geomagnetic cutoff rigidities for Earth-orbiting spacecraft. *Adv. Space Res.* **36**, 2012. DOI.
Subramanian, P., Antia, H.M., Dugad, S.R., Goswami, U.D., Gupta, S.K., et al. (Grapes-3 Collaboration): 2009, Forbush decreases and turbulence levels at coronal mass ejection fronts. *Astron. Astrophys.* **494**, 1107. DOI.
Thébault, E., Finlay, C.C., Beggan, C.D., et al.: 2015, International geomagnetic reference field: the 12th generation. *Earth Planets Space* **67**, 79. DOI.
Venkatesan, D., Badruddin: 1990, Cosmic-ray intensity variations in the 3-dimensional heliosphere. *Space Sci. Rev.* **52**, 121. DOI.
ROOT-website (2015): https://root.cern.ch/doc/master/classTVirtualFFT.html.

Authors and Affiliations

C. Alvarez[1] · J.R. Angeles Camacho[2] · J.C. Arteaga-Velázquez[3] · K.P. Arunbabu[4,5] · D. Avila Rojas[2] · V. Baghmanyan[6] · E. Belmont-Moreno[2] · S.Y. BenZvi[7] · C. Brisbois[8] · K.S. Caballero-Mora[1] · T. Capistrán[9] · P. Colín-Farias[4] · U. Cotti[3] · J. Cotzomi[10] · S. Coutiño de León[9] · E. De la Fuente[11] · S. Dichiara[12] · B.L. Dingus[13] · M.A. DuVernois[14] · J.C. Díaz-Vélez[11] · C. Espinoza[2] · N. Fraija[12] · A. Galván-Gámez[12] · D. Garcia[2] · J.A. García-González[2] · F. Garfias[12] · M.M. González[12] · J.A. Goodman[15] · J.P. Harding[13] · S. Hernandez[2] · B. Hona[8] · D. Huang[8] · F. Hueyotl-Zahuantitla[1] · A. Iriarte[12] · V. Joshi[16] · G.J. Kunde[13] · A. Lara[4] · H. León Vargas[2] · A.L. Longinotti[9] · G. Luis-Raya[17] · K. Malone[13] · O. Martinez[10] · J. Martínez-Castro[18] · J.A. Matthews[19] · P. Miranda-Romagnoli[20] · J.A. Morales-Soto[3] · E. Moreno[10] · A. Nayerhoda[6] · L. Nellen[21] · M. Newbold[22] · R. Noriega-Papaqui[20] · A. Peisker[23] · Y. Pérez Araujo[12] · E.G. Pérez-Pérez[17] · C.D. Rho[7] · D. Rosa-González[9] · M. Rosenberg[24] · J. Ryan[25] · H. Salazar[10] · A. Sandoval[2] · R.W. Springer[22] · E. Tabachnick[15] · O. Tibolla[17] · K. Tollefson[23] · I. Torres[9] · R. Torres-Escobedo[11] · L. Villaseñor[10] · A. Zepeda[26] · H. Zhou[1] · C. de León[3]

✉ K.P. Arunbabu
arun@igeofisica.unam.mx

✉ A. Lara
alara@igeofisica.unam.mx

1 Universidad Autónoma de Chiapas, Tuxtla Gutiérrez, Chiapas, Mexico

2 Instituto de Física, Universidad Nacional Autónoma de México, Mexico City, Mexico

3 Universidad Michoacana de San Nicolás de Hidalgo, Morelia, Mexico

4 Instituto de Geofísica, Universidad Nacional Autónoma de México, Mexico City, Mexico

5 Department of Physics, St. Paul's College, Kalamassery, Kerala, India

6 Institute of Nuclear Physics, Polish Academy of Sciences, IFJ-PAN, 31342, Krakow, Poland

7 Department of Physics & Astronomy, University of Rochester, Rochester, NY, USA

8 Department of Physics, Michigan Technological University, Houghton, MI, USA

9 Instituto Nacional de Astrofísica, Óptica y Electrónica, Puebla, Mexico

10 Facultad de Ciencias Físico Matemáticas, Benemérita Universidad Autónoma de Puebla, Puebla, Mexico

11 Departamento de Física, Centro Universitario de Ciencias Exactas e Ingenierías, Universidad de Guadalajara, Guadalajara, Mexico

12 Instituto de Astronomía, Universidad Nacional Autónoma de México, Mexico City, Mexico

13 Physics Division, Los Alamos National Laboratory, Los Alamos, NM, USA

14 Department of Physics, University of Wisconsin-Madison, Madison, WI, USA

15 Department of Physics, University of Maryland, College Park, MD, USA

16 Erlangen Centre for Astroparticle Physics, Friedrich-Alexander-Universität Erlangen-Nürnberg, Erlangen, Germany

17 Universidad Politécnica de Pachuca, Pachuca, Hidalgo, Mexico

18 Centro de Investigación en Computación, Instituto Politécnico Nacional, Mexico City, Mexico

19 Dept. of Physics and Astronomy, University of New México, Albuquerque, NM, USA

20 Universidad Autónoma del Estado de Hidalgo, Pachuca, Mexico

21 Instituto de Ciencias Nucleares, Universidad Nacional Autónoma de México, Mexico City, Mexico

22 Department of Physics and Astronomy, University of Utah, Salt Lake City, UT, USA

23 Department of Physics and Astronomy, Michigan State University, East Lansing, MI, USA

24 Department of Physics, Pennsylvania State University, University Park, PA, USA

25 Space Science Center, University of New Hampshire, Durham, NH, USA

26 Physics Department, Centro de Investigación y de Estudios Avanzados del IPN, Mexico City, Mexico